

Analysis of Lifetime-Limiting Defects in Cast-Mono Silicon Using Injection-Dependent Lifetime Spectroscopy Methods

Raphael Cabal^{ID}, Nicolas Enjalbert, Sylvain Rousseau, and Sébastien Dubois

Abstract—Seed-assisted cast-mono silicon for photovoltaic (PV) application is a relevant alternative to the conventional Czochralski (Cz) in terms of cost and carbon footprint. Despite the remarkable PV conversion efficiencies reached when combining this material with novel cell concepts, cast-mono industrial deployment is infringed by the propagation of dislocation clusters during crystallization, inducing variations in final wafers quality. Indeed, some wafers feature dislocation-rich regions whose recombination activity is not fully understood. This article aims at providing insights into the carrier recombination in such regions. We focus on n-type cast mono grown from a compensated feedstock in order to obtain samples with the same crystallographic properties but different electron concentration (n_0) values. The bulk carrier lifetime in the dislocation-rich region could be approximated by the combination of two discrete defects for which the symmetry factor k could be estimated first by exploiting the relationship between the defect lifetime gradient with $1/n_0$. Both defects energy positions (E_T) could be obtained, thanks to the defect parameter surface solution method. We analyzed the variations of the first defect Shockley–Read–Hall (SRH) parameters (E_T , k , and hole lifetime constant τ_{p0}) with n_0 and for temperatures ranging from 30 to 75 °C. A temperature-assisted transition of the first defect from one state to another was highlighted and was found to be enhanced by low n_0 values. For each state, the SRH parameters were extracted.

Index Terms—Characterization of defects in photovoltaic (PV), crystalline silicon photovoltaic (PV), lifetime spectroscopy.

I. INTRODUCTION

SEED-ASSISTED cast-mono silicon for solar cells has shown significant progress with increasingly higher reported photovoltaic (PV) conversion efficiencies comparable with those of mass production Czochralski (Cz) cells [1], [2]. Nevertheless, cast-mono silicon still suffers from the presence of dislocations capping the performance of PV solar cells originating from the upper part of the ingot. In dislocated regions, the effective carrier lifetime (τ_{eff}) can be more than two orders of magnitude lower than the values found in the nondislocated regions of the same wafer [3]. While the exact root cause

for dislocation generation is not comprehensively understood, the plastic deformation introduced at seed surfaces/joints by thermomechanical stress is surely involved [4]. Solutions were proposed in the literature to avoid or at least mitigate the dislocations propagation, such as the use of hardening elements [5] or buffer silicon pellets/wafers to protect Cz seeds from indentation [6]. However, a complete and systematic suppression of dislocations at an industrial scale has not been reported so far. At the cell level, a promising approach to mitigate the recombination strength of dislocations is based on the additional hydrogenation processes [7]. Nevertheless, even after such treatments, the final bulk lifetime in dislocated regions remains generally one order of magnitude lower than the value found in dislocation-free regions. In addition, various dislocated regions may not respond the same way to one given hydrogenation treatment [8], probably depending on the nature and spatial distribution of the metallic impurities decorating the dislocation. The recombination activity of the dislocation/impurity combination raises complex issues, many impurities being likely to precipitate or occupy substitutional/interstitial sites along the dislocations. The use of an external gettering may be relevant to detect metal impurities initially located in the dislocation-rich regions and ultimately back quantifying them using, for instance, secondary ion mass spectrometry [9]. However, this procedure does not provide any information regarding the influence of the extracted elements on the recombination strength of the dislocation. Furthermore, the gettering treatment may also modify the metal impurities distribution in the dislocation-rich regions known to provide preferential sites for impurity accumulation. The identification of metal impurities by X-ray fluorescence or inductively coupled plasma mass spectrometry may be impeded by detection limits above the usual levels of metal impurity concentrations found in cast-mono samples. The advanced local characterization techniques, such as atom-probe tomography, provide the accurate quantification of the existing impurities yet only very locally, inducing the risk that the detected impurities may not be the one governing the macroscopic performance [10]. Conversely, injection-dependent lifetime spectroscopy (IDLS) is an easy-to-implement method known to detect defects related states even at low concentration levels [11]. In this article, we apply IDLS procedures to dislocated regions of cast mono. In such regions, τ_{eff} is usually dominated by the bulk contribution (τ_{bulk}). Here, we consider the possibility to approximate the overall carrier recombination in cast-mono dislocated regions by

Manuscript received October 30, 2020; revised January 15, 2021, March 9, 2021, and April 2, 2021; accepted April 6, 2021. (Corresponding author: Raphael Cabal.)

The authors are with the University Grenoble Alpes, CEA, LITEN, DTS, INES, F-38000 Grenoble, France (e-mail: raphael.cabal@cea.fr; nicolas.enjalbert@cea.fr; sylvain.rousseau@cea.fr; sebastien.dubois@cea.fr).

Color versions of one or more figures in this article are available at <https://doi.org/10.1109/JPHOTOV.2021.3074060>.

Digital Object Identifier 10.1109/JPHOTOV.2021.3074060

Shockley–Read–Hall (SRH) recombination through a set of predominant discrete energy levels over a wide range of samples electron densities (n_0). This point-defect-oriented approach is motivated by studies indicating that the clouds of point defects surrounding the dislocations are influencing the dislocation recombination activity [12], being, for example, responsible for a modification of dislocations deep-level transient spectroscopy C line signature [13]. The n-type cast-mono ingot studied here exhibits a resistivity ranging from 4 to 27 $\Omega\cdot\text{cm}$ due to an intentional compensation of the ingot doping by boron atoms. We measured injection-dependent τ_{eff} curves by quasi-steady-state photoconductance (QSSPC) on dislocation-rich regions of wafers taken from the upper part of the ingot. The signal measured by QSSPC can be seen as an apparent macroscopic response involving the multiple defects at play. The methodology used here consists of doing the following:

- 1) applying a linearization process to isolate up to two independent defect contributions to the SRH lifetime;
- 2) applying IDLS to the defect-limited terms (τ_D) for different conditions of n_0 and temperature (T); and
- 3) building the it is actually defect parameter solution surface (DPSS) [14] to determine the energy (E_T), the symmetry factor (i.e., the capture cross-sections ratio, k), as well as the hole lifetime constant (τ_{p0}) of the defect. A similar approach was proposed in [15] to characterize the recombination in both dislocation-rich and dislocation-free regions of a high-performance multicrystalline wafer, using exclusively T -IDLS. In the present work, we combine both n_0 and T variations.

II. EXPERIMENTAL DETAILS

A. Preliminary Verifications

The surfaces of the tested silicon wafers were electrically passivated with an $\text{AlO}_x\backslash\text{SiN}_y:\text{H}$ stack, known to provide sufficiently low surface recombination velocity (S) and weak injection dependence at low-injection level [16], as well as good thermal stability. The values of S provided by this $\text{AlO}_x\backslash\text{SiN}_y:\text{H}$ stack are known to be particularly low on dislocation-free Cz silicon ($S < 10 \text{ cm/s}$). However, as we focus here on the dislocation-rich regions of cast-mono wafers, we first revisited the values of S in that specific case. A standard (noncompensated) n-type cast-mono brick was used for S extraction. Alike the compensated ingot devoted to the IDLS procedures, the brick upper part featured homogeneously distributed dislocations with a comparable subgrain size. A specific sawing setup was used, resulting in alternate wafer thicknesses (W) of 150 and 220 μm , well suited to S extraction. For these samples, the electron concentration was $n_0 = 2.0 \times 10^{15} \text{ cm}^{-3}$, slightly higher than the n_0 values of the IDLS samples. After RCA cleaning, surface passivation ($\text{AlO}_x\backslash\text{SiN}_y:\text{H}$), and firing, τ_{eff} was measured at room temperature on samples with different thicknesses. Equation (1), as proposed by Grivickas *et al.* [17], was used to calculate S and the deviation between the effective and bulk lifetimes (D being the minority carrier diffusion coefficient). The dynamics of S was almost flat on the $[10^{15} - 5 \times 10^{16}] \text{ cm}^{-3}$ injection range with values of $26 \pm 3 \text{ cm/s}$ after firing. S values are above those usually

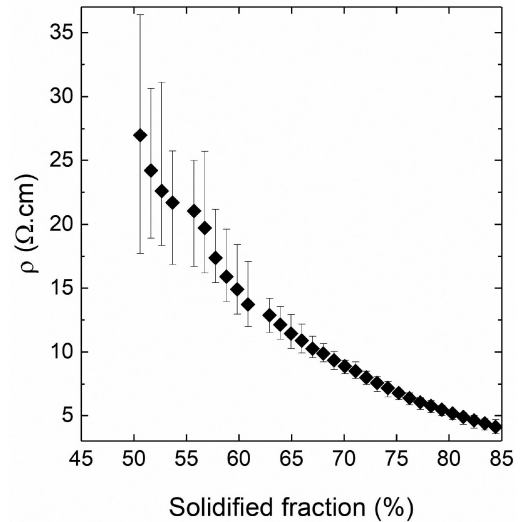


Fig. 1. Wafer average resistivity from 4 point probe mapping as a function of the solidified fraction.

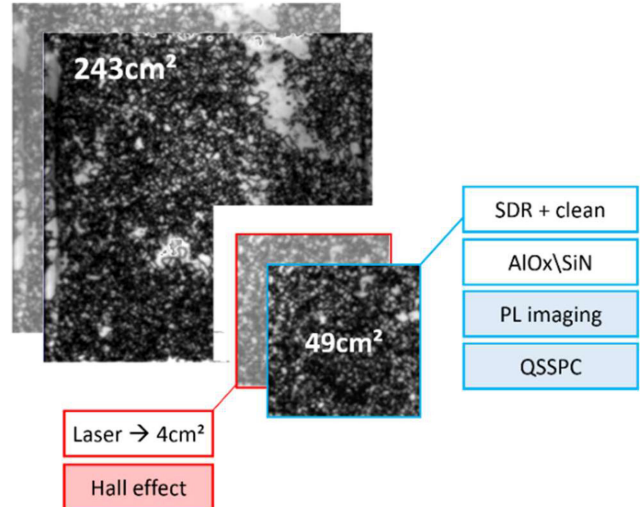


Fig. 2. PL images of the studied wafers. For each considered position along the ingot, the IDLS (in blue) and Hall effect samples (in red) were selected from the dislocation-rich region (49 cm^2 area) of two consecutive wafers.

obtained on dislocation-free silicon. However, the deviation between τ_{eff} and τ_{bulk} remains below 8% on the investigated injection range, which makes τ_{eff} a decent approximation of τ_{bulk} in the defective regions of interest in this study.

$$\frac{1}{\tau_{\text{eff}}} = \frac{1}{\tau_{\text{bulk}}} + \left(\frac{W}{2S} + \frac{1}{D} \left(\frac{W}{\pi} \right)^2 \right)^{-1}. \quad (1)$$

B. Sample Processing

We chose to work on a specific n-type cast-mono ingot featuring a large resistivity (ρ) variation in order to exploit SRH n_0 dependence. The drastic drop in ρ observed in the upper part of the ingot (see Fig. 1) was made possible by using a boron–phosphorus compensated Si feedstock.

The interpretation of lifetime spectroscopy outputs is easier when the procedure is applied to samples featuring one homogeneously distributed set of dominating defects. Obtaining a neat intersection of DPSS batches is favored by T independent k (or n_0 independent τ_{p0}). Our material advantageously features a steep drop in ρ , running along a narrow solidified fractions range (65–85%) and, therefore, along a small part of the ingot. For this reason, the samples extracted from this region of the ingot feature similar crystallographic properties (i.e., dislocation type, density, and distribution). The equivalence of our samples in terms of compositional properties is more questionable. Regarding the possible change in metal impurities contents along the studied part of the ingot, the Scheil equation is incomplete for an accurate description of the variation of the metal elements concentrations along the ingot height (e.g., it does not take into account the solid-state diffusion during the cooling of the ingot). For this reason, we rather considered the experimental data from the literature. In the present work, we will focus on ungettered wafers taken between 65% and 85% of solidified fractions. Previous studies showed that the iron concentration, iron being one of the most abundant metal element in cast Si, should not significantly vary in this range of solidified fractions: increases from 1.5×10^{14} to $4.0 \times 10^{14} \text{ cm}^{-3}$ and from 9.5×10^{12} to $1.3 \times 10^{13} \text{ cm}^{-3}$, were reported for total and interstitial iron (Fe_i) concentrations, respectively [18], [19]. Considering such small variations as negligible is a statement whose validity will be discussed in Section III-D.

The studied brick was cut into $180 \mu\text{m}$ thick wafers that experienced a saw-damage removal step followed by a RCA cleaning? They were double-side passivated by the aforementioned stack of $\text{AlO}_x \backslash \text{SiN}_y : \text{H}$, then submitted to a firing step ($T_{\text{peak}} = 885^\circ\text{C}$). IDLS requires high precision in the τ_{eff} data. For this reason, the QSSPC measurements were performed on as homogeneous as possible selected regions of the wafers. Images of the room- T PhotoLuminescence (PL) signal of the passivated wafers and ρ mappings were used as a guide for selecting the relevant region combining a uniform intra-wafer resistivity with homogeneous crystallographic properties. For each position along the ingot, two consecutive wafers were taken from which the 49 cm^2 samples corresponding to the relevant region were cut by laser, as illustrated in Fig. 2. The first one was used for IDLS, while 4 cm^2 squared subsamples were cut out the second one, once again by laser, and dedicated to n_0 measurement by Hall effect.

C. Hall Effect and Photoluminescence

Ohmic contacts were deposited at each corner of the 4 cm^2 samples, using a liquid Indium–Gallium eutectic forced through the Si surface with a diamond pin. The assessments of the Hall electron density ($n_H = n_0/r_H$) were conducted at 300 K. The n-type silicon Hall factor r_H is assumed here to be not influenced by the dopant compensation, analogically to what was reported for p-type Si [20]. We used for r_H a value of 1.15 in agreement with the data reported at 300 K for noncompensated n-type Si [21]. The resulting values of n_0 are reported in Fig. 3 for four sample positions along the ingot (i.e., solidified fractions). Prior

to firing and further analysis, the IDLS samples (49 cm^2) were submitted to room temperature PL imaging in order to assess the signal uniformity within the center region facing the active sensor area of the QSSPC equipment. The global PL response of the studied dislocation-rich region (reported in Fig. 3) presents the comparable signal distributions from one sample position to another.

D. Lifetime Testing

A Sinton WCT-120 TS unit was used for the QSSPC measurements performed on the 49 cm^2 samples between 25 and 80°C with a 5°C step. This reduced temperature range was used to avoid any permanent annealing effect, which was verified by performing a reference QSSPC measurement at room- T before and after each temperature scan. Since the mobility model in the standard Sinton datasheet is not suited for compensated material, we used the Sinton setup to measure the generation rate (G) and the conductivity variation ($\Delta\sigma$). For each sample position, the compensation level at room temperature $C_{l,RT}$ defined by $(N_A + N_D)/(n_0 + p_0)$ is reported in Fig. 3, where N_A and N_D being the acceptor and donor concentrations, respectively. $C_{l,RT}$ was computed from the boron and phosphorus concentrations ([B] and [P]) added to the feedstock and by using the Scheil law to assess the [B] and [P] distributions along the height of the ingot. The excess carrier concentration (Δn) was calculated afterward using (2) in which the electron and hole mobilities (μ_n , μ_p) provided by Schindler's model [22] were implemented (taking into account the previously computed [B] and [P]). Eventually, $\tau_{\text{eff}} (= \frac{\Delta n}{G})$ could be derived. The uncertainty on the lifetime measurement was not included in the section III calculations and we used exclusively averaged lifetime data resulting from a ten consecutive flashes measurement. As the n_0 values of the IDLS samples are slightly lower than the n_0 of the sample used to extract S , and as both types of samples feature similar crystallographic properties, the previously calculated values can be used as an upper limit of S and show that τ_{eff} is a decent approximation for τ_{bulk} (<8% error). After correcting τ_{bulk} from intrinsic and Auger contributions, we obtain the residual SRH component (τ_{SRH}).

$$\Delta n = \frac{\Delta\sigma}{q(\mu_n + \mu_p)}. \quad (2)$$

E. Iron–Boron Pairs

Cast silicon materials usually contain significant concentrations of iron. Furthermore, the n-type material studied here is compensated (i.e., the presence of boron atoms). Fe_i could interact with boron by forming metastable FeB pairs. The formation/dissociation of the FeB pairs could induce carrier lifetime changes interfering with the mathematical treatments of the QSSPC data and their interpretation. Therefore, particular attention was paid to such acceptor-related defects. Kimerling and Benton [23] showed that the association/dissociation of the FeB pairs is controlled by electronic mechanisms. Therefore, as in compensated n-type silicon, the charge state of Fe_i is neutral,

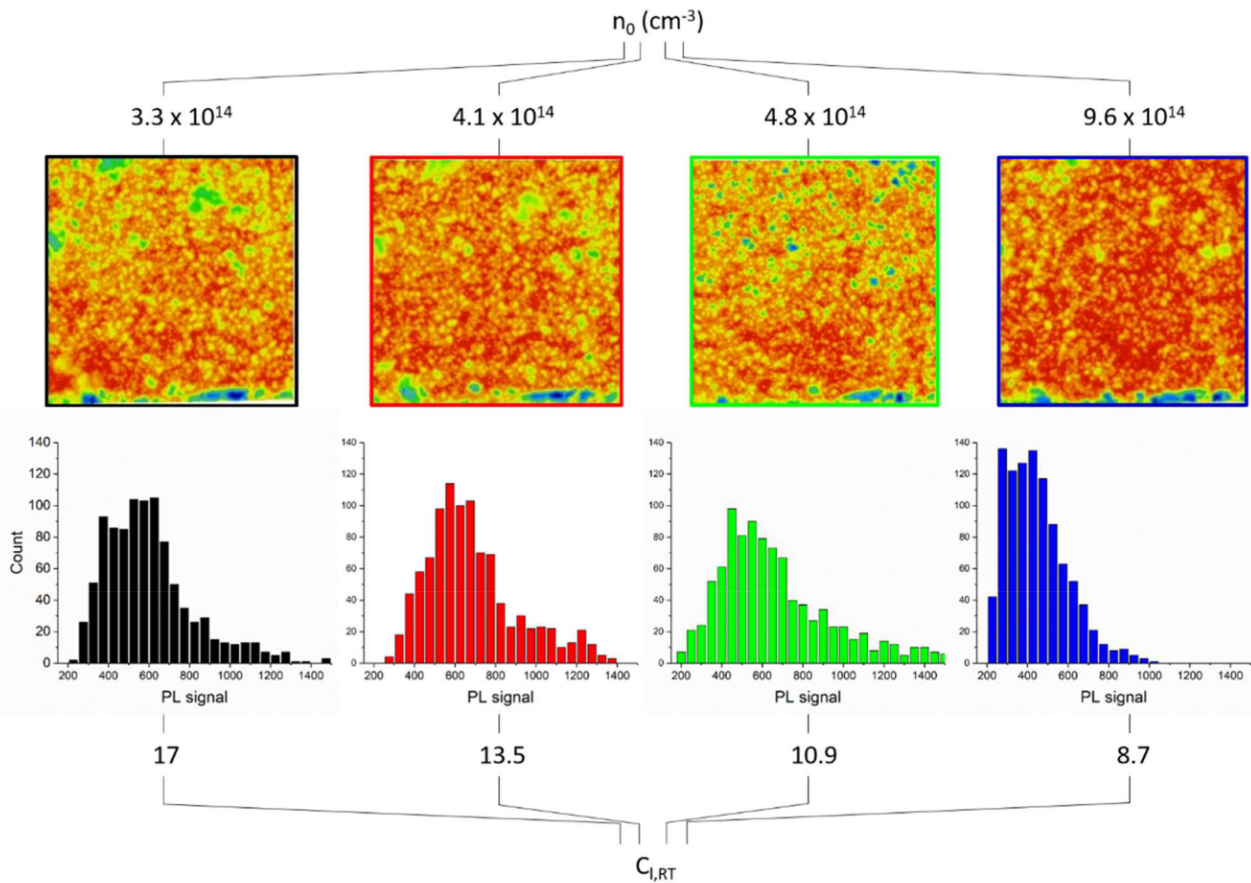


Fig. 3. Top to bottom: the electron concentration n_0 computed from Hall effect measurement; the IDLS samples PL images and the corresponding signal distribution (within the Sinton sensor area); the compensation level at room-T ($C_{l,RT}$).

and FeB pairs should not be present. This feature was experimentally observed by Kimerling and Benton [23] in reverse-biased boron-doped p-type silicon. However, more recently Rougieux *et al.* [24] investigated the possibility of such reactions by carrier lifetime measurements before and after the illumination of two iron-containing n-type compensated samples featuring different resistivity values. Regarding the sample with the lower resistivity, as expected, the carrier lifetime was not influenced by the illumination. Concerning the sample with the higher resistivity, unexpected slight changes of the carrier lifetime were observed, particularly at high-injection levels. Various explanations were proposed (e.g., steric effects, inhomogeneities in the type of conductivity) and the authors claimed that further analyses would be needed in order to validate the presence of FeB pairs in compensated n-type silicon. Thus, the potential formation of FeB pairs in such materials is still an open question.

In order to investigate the sensitivity of our compensated n-type samples to changes in carrier lifetime due to possible associations/dissociations of the FeB pairs, we conducted repeated microwave detected PhotoConductance decay (μ W-PCD) carrier lifetime measurements in the dislocation-rich regions by using a procedure similar to the one used to determine the Fe_i concentration in p-type samples [25]. The laser pulse required for the μ W-PCD measurement acts as an illumination source for dissociating the FeB pairs. This procedure was conducted

for the compensated samples with the highest and lowest n_0 (n_0 values equal to 9.6×10^{14} and $3.3 \times 10^{14} \text{ cm}^{-3}$, respectively). Fig. 4(a) presents the obtained results. Interestingly, for both samples, slight increases of the carrier lifetime were highlighted, suggesting a dissociation of the FeB pairs. With p-type silicon, if the material is kept in the dark at room temperature, the FeB pairs reassociate. We conducted repeated μ W-PCD carrier lifetime measurements in another location within the dislocation-rich region of the compensated n-type cast-mono sample with $n_0 = 3.3 \times 10^{14} \text{ cm}^{-3}$. Fig. 4(b) presents the obtained results.

In part i) of the graph, continuous repeated measurements were applied, confirming the slight increase of the carrier lifetime pointed out in Fig. 4(a). Then, in part ii), the sample was kept in the dark between the several short series of measurements. It can be observed that the carrier lifetime drops back to its original value, similarly to the effect of the FeB pairs reformation in p-type Si. Thus, these results would confirm the hypothesis from Rougieux *et al.*, namely the formation of FeB pairs in compensated n-type silicon, even if further studies would be necessary to fully validate this result. Indeed, the presence of other defects than FeB pairs behind these carrier lifetime changes cannot be ruled out completely. During the repeated μ W-PCD measurements, as shown in Fig. 4(a), the carrier lifetime only changed by 2.6% for the sample with $n_0 = 9.6 \times 10^{14} \text{ cm}^{-3}$ and by 6.2% for the sample with $n_0 = 3.3 \times 10^{14} \text{ cm}^{-3}$.

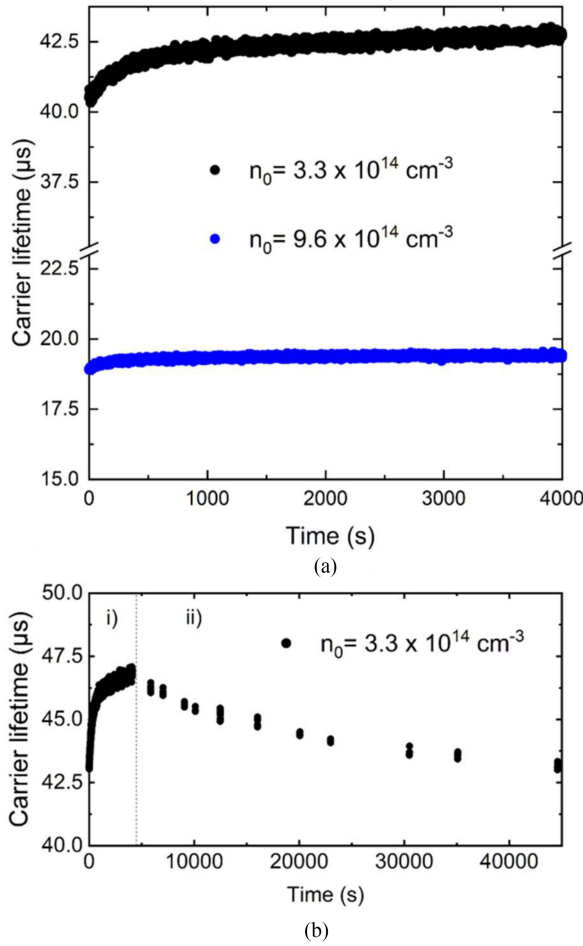


Fig. 4. Evolution of the carrier lifetime during repeated μ W-PCD measurements. Graph a) and Graph b) part i): measurements were continuously repeated. Graph b) part ii): sample was kept in the dark between several short series of repeated measurements.

The carrier lifetime changes due to FeB pairs association/dissociation occurring during the QSSPC measurement protocol should be lower than these variations. Indeed, the repeated μ W-PCD measurements have been conducted during a relatively long period of time (higher than 1 h), and the carrier lifetime data extracted with the μ W-PCD measurement setting correspond to high-injection values (according to the data from Rougier *et al.*, the effect of FeB pairs dissociation on the carrier lifetime in compensated n-type silicon would be stronger at high injection) [24]. Therefore, the influence of the association/dissociation of FeB pairs on the carrier lifetime spectroscopy procedures presented here should only be minor. This is also in accordance with the aforementioned fact that the reference QSSPC measurements at room- T before and after each temperature scan gave similar results.

III. INJECTION-DEPENDENT LIFETIME SPECTROSCOPY

A. SRH Defect Isolation Process

After deriving τ_{SRH} from τ_{eff} QSSPC measurements, one must identify the predominant SRH defects at play. Murphy

et al. proposed to use the SRH lifetime in its linear form (i.e., expressed as a function of the minority to majority carrier densities ratio; here, $Y = \frac{p}{n}$) in order to facilitate the isolation of one or two separate defects dominating the overall SRH lifetime. When using the SRH statistics, we assume that the carrier lifetime is governed by independent single-level defects. In the defect isolation process, each individual defect-related lifetime (τ_D) is an affine function of Y , as presented in (3), where (N_C and N_V) are the densities of states in the conduction/valence bands, and (σ_n and σ_p) are the capture cross sections for electrons/holes

$$\tau_D = \frac{1}{\alpha_p N_T} \left[1 + \frac{n_1}{n_0} + \frac{p_1}{n_0 Q} + Y \left(\frac{1}{Q} - \frac{n_1}{n_0} - \frac{p_1}{Q n_0} \right) \right] \quad (3)$$

with $n_1 = N_C e^{-\left(\frac{E_C-E_T}{k_B T}\right)}$, $p_1 = N_V e^{-\left(\frac{E_T-E_V}{k_B T}\right)}$ and $Q = \frac{\alpha_n}{\alpha_p} = \frac{\sigma_n v_{\text{th}}(e)}{\sigma_p v_{\text{th}}(h)} = k \frac{v_{\text{th}}(e)}{v_{\text{th}}(h)}$.

In the present article, the room- T thermal velocities for electron and hole are $v_{\text{th}}(e) = 2.1 \times 10^7 \text{ cm/s}$ and $v_{\text{th}}(h) = 1.7 \times 10^7 \text{ cm/s}$, respectively. Under high injection (i.e., for $Y \rightarrow 1$), (3) can be simplified to

$$\tau_{D(Y \rightarrow 1)} = \frac{1}{\alpha_p N} \left(1 + \frac{1}{Q} \right). \quad (4)$$

Eventually, when dividing the defect-related lifetime gradient ($\frac{d\tau_D}{dY}$) by the lifetime limit at high injection, the resulting quantity is an affine function of the reciprocal of the equilibrium electron density ($\frac{1}{n_0}$), as expressed in (5). From the intercept of this affine function, the capture coefficient ratio (Q) and ultimately the capture cross-sections ratio k ($= \frac{\sigma_n}{\sigma_p}$) can be deduced. Once Q is determined, the energy position (E_T) is calculated from the slope of the affine function.

$$\left(\frac{d\tau_D}{dY} \right) / \tau_{D(Y \rightarrow 1)} = \frac{1}{1+Q} - \frac{1}{n_0} \left(\frac{n_1 + \frac{p_1}{Q}}{1+Q} \right). \quad (5)$$

B. Defect Parameter Solution Surface

Assuming equal excess electron and hole concentrations ($\Delta n = \Delta p$), the contribution of a given single-level defect to SRH lifetime is expressed as follows:

$$\tau_D = \tau_{p0} \left(\frac{p_0 + p_1 + \Delta p}{k(p_0 + n_0 + \Delta p)} + \frac{n_0 + n_1 + \Delta p}{p_0 + n_0 + \Delta p} \right). \quad (6)$$

The defect is defined by its set of SRH parameters (E_T , k , and hole capture time constant τ_{p0}). Different sets of SRH parameters may allow a good fit of the previously isolated lifetime curves each associated with a single level. The defect parameter solution surface (DPSS), as proposed by Rein [14], consists in finding the best fitting pair of values for $(k; \tau_{p0})$ for a given E_T . The DPSS of a single lifetime curve still results in a broad range of least-square fit minima associated with a broad range of parameter solutions. A way to overcome the remaining ambiguity on the defect parameters is to perform the DPSS routine on a set of lifetime curves obtained at different T (T-IDLS) or using different sample doping concentrations (n_0 -IDLS). A set of DPSS curves obtained from n_0 or T-IDLS ideally features only two crossing points, where the curves intersect, corresponding to the recurrent best fitting SRH parameter values,

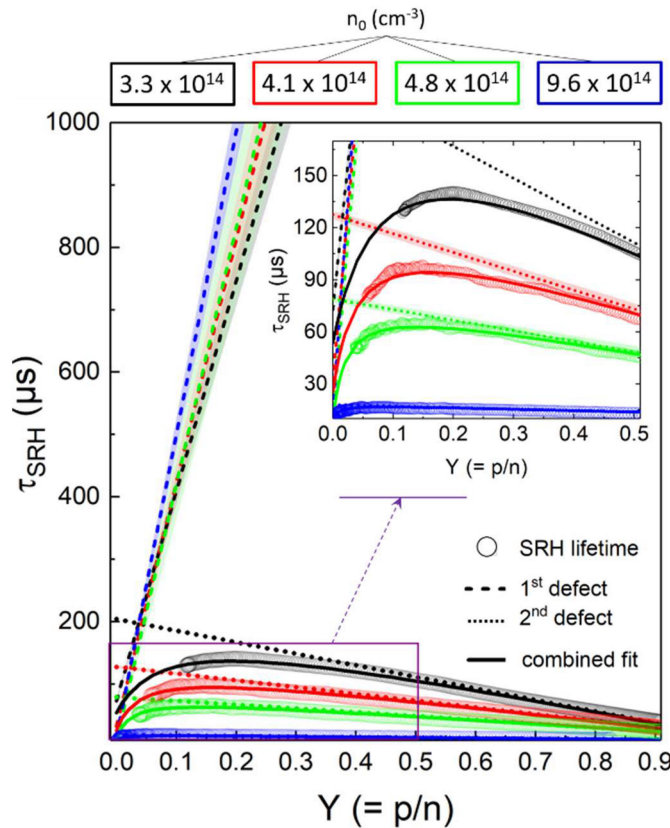


Fig. 5. SRH lifetime measured at 30 °C on samples with different electron density (n_0) values and plotted versus p/n. The experimental lifetime curves are shown as open circles. The contributions of the first and second defects (dashed and dotted lines, respectively) and their combination (solid lines) are also shown.

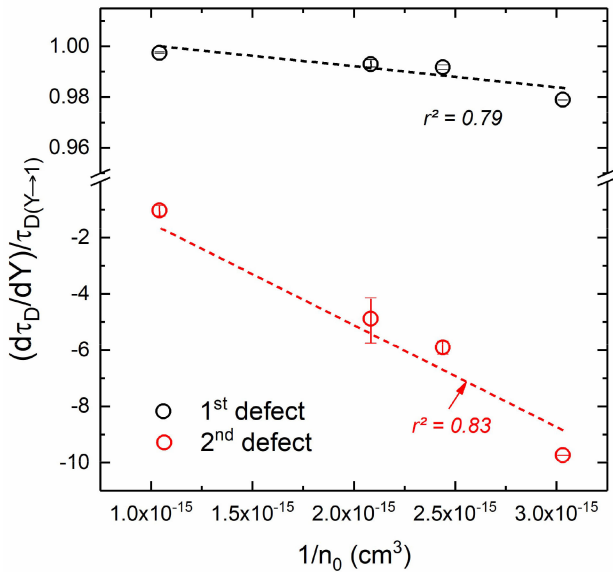


Fig. 6. Gradients of defect-limited lifetime divided by the lifetime limit ($Y \rightarrow 1$) and plotted versus the reciprocal of the equilibrium electron density. The error bars resulting from individual defect lifetime parameterization uncertainties during the isolation process are also shown. The dashed lines are linear regressions of the displayed data.

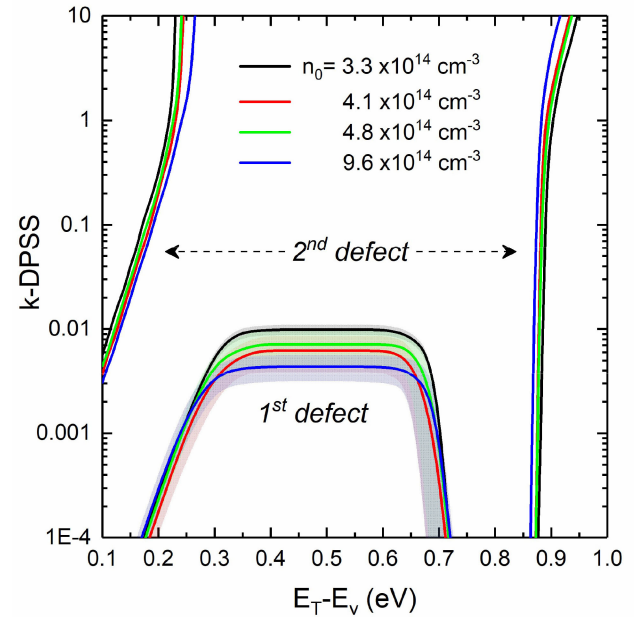


Fig. 7. k -DPSS at 30 °C on samples with different equilibrium electron densities (n_0) for the first and second defects. The first defect continuous DPSS curves (solid lines) are surrounded by error bands induced by the isolation process uncertainties. The second defect exhibits discontinuous DPSS defined near the band edges.

and detected, thanks to relative standard deviation (RSD in %) minimization. This allows $(k; \tau_{p0})$ to be determined and the reduction of E_T to two most probable solutions, one in each half of the bandgap. DPSS constructed for the symmetry factor and hole capture time constant will be referred to as k -DPSS and τ_{p0} -DPSS, respectively. Determining k from the perfect intersection of k -DPSS curves obtained from a set of T -IDLS data implies that k is T -independent, which is not granted since the electron and hole capture cross sections may vary differently with T . For this reason, we will focus first on k -DPSS obtained from n_0 -IDLS data since k is theoretically independent of the substrate doping.

C. Room Temperature (n_0 -IDLS)

The defect isolation process was applied to the IDLS samples at $T = 30$ °C, 45 °C, 60 °C, and 75 °C. The strict room- T (25 °C) was discarded because we wanted the sample T to be strictly imposed by the Sinton tester heating chuck in order to avoid the influence of possible variations in the clean room temperature. For each condition of n_0 and T , the contributions of two single-level defects could be distinguished using the isolation process. One should stress here that the SRH lifetime may be affected by more defects than the two identified here. However, the procedure is not able to extract the contributions of more than two defects. The first defect exhibits systematically a positive slope and is affecting τ_{SRH} at low injection, while the second defect exhibits a negative slope and governs the intermediate and high-injection levels.

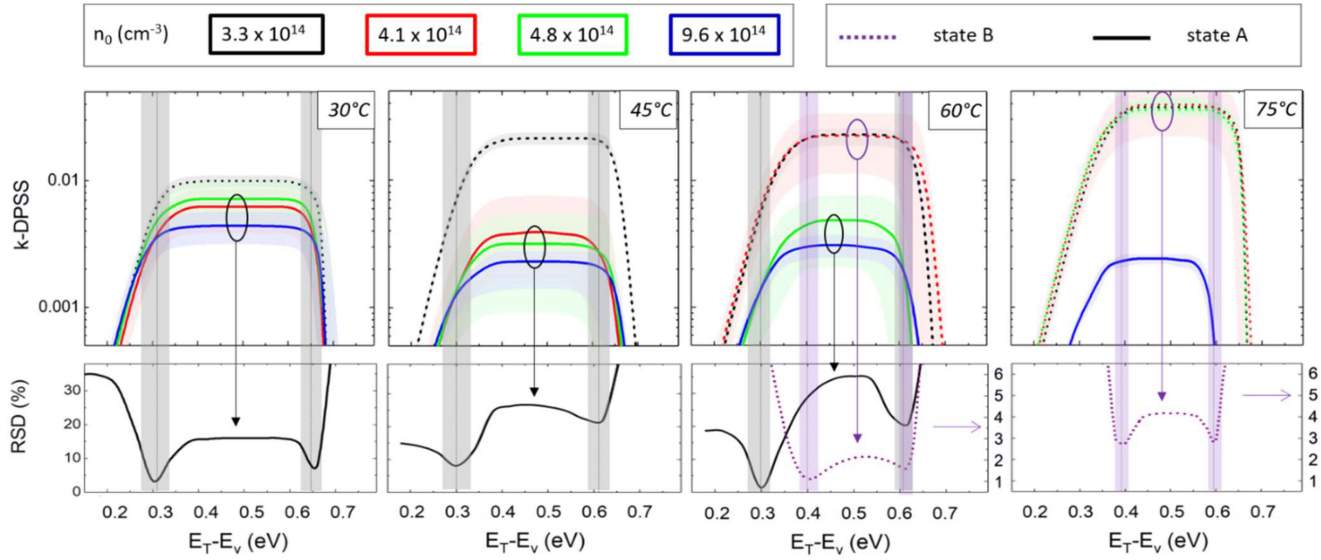


Fig. 8. (Top) k -DPSS constructed from first defect lifetime best fits, for different samples equilibrium electron densities (n_0 -IDLS method). From left to right, the data were collected at temperatures ranging from 30 to 75 °C; (bottom) the corresponding RSD plots calculated in both state A (solid lines) and state B (dashed lines) cases.

Fig. 5 plots the result of the isolation procedure for $T = 30$ °C for different n_0 . For each defect, the τ_{SRH} versus Δn affine functions are plotted and surrounded by the isolation procedure-related error bands. As can be seen from these error bands, the parameterization of the first defect suffered a larger uncertainty (up to 16%) owing to the fact that this defect governs only a small portion of the measured injection level range. The uncertainty for the second defect was much smaller (4.9% in the worst case). Fig. 6 presents the $(\frac{d\tau_D}{dY})/\tau_{D(Y \rightarrow 1)}$ quantity plotted against $(\frac{1}{n_0})$ for the first and second defects based on the data collected at 30 °C. The r -squared (r^2) value of the linear regression of each affine function (0.79 and 0.83 for the first and second defect, respectively) is reported in the figure.

Q values were extracted from the intercept of each affine function, and k was eventually derived. The first defect has a symmetry factor k equal to 0.007 ± 0.001 . A slight deviation of the value (i.e., gradient divided by the lifetime limit) computed for the sample with the lowest doping level ($n_0 = 3.3 \times 10^{14}$ cm⁻³, i.e., $1/n_0 = 3.0 \times 10^{-15}$ cm³ on the graph) was noticed. E_T extraction from the affine function slope gave the following values $E_v + 0.39 \pm 0.09$ eV or $E_v + 0.68 \pm 0.06$ eV. The second defect exhibits a weaker asymmetry with k equal to 0.60 ± 0.03 . The determination of E_T was in that case more accurate ($E_v + 0.23 \pm 0.03$ eV or $E_v + 0.90 \pm 0.02$ eV). In this work, we performed the DPSS routines on each defect isolated lifetime one by one. The k -DPSS curves constructed for both the first and second defects from n_0 -IDLS data measured at 30 °C are presented in Fig. 7. The first defect DPSS curves are mean values together with the corresponding error bands induced by the uncertainties inherent from the aforementioned defect isolation process. These curves exhibit a plateau with reasonably well-defined intersections, except for the DPSS in black that corresponds to the sample with $n_0 = 3.3 \times 10^{14}$ cm⁻³. This sample behaves singularly in the same fashion as what was

observed in Fig. 6. This deviation and its impact on $(E_T; k; \tau_{p0})$ determination will be further discussed in Section III-D. The DPSS for the second defect features a split range for each temperature investigated here (not shown).

D. Temperature-Dependent Results

For a given n_0 , the determination of SRH parameters from T -IDLS is not presented here. The intersection of DPSS curves constructed at different T was indeed rather broad, which can be the combined result of the aforementioned uncertainties, with some T -dependence of k and τ_{p0} (via the hole capture cross section). We focused instead on the n_0 -IDLS DPSS curves intersection, one temperature condition after the other, as presented in Fig. 8.

The deviation previously reported in the case of $n_0 = 3.3 \times 10^{14}$ cm⁻³ was observed at higher temperatures and is likely related to some T -assisted defect transitions. Indeed, the analysis of the first defect lifetime k -DPSS curves evidenced an unexpected shift from a predominant state A to a predominant state B, the first one being defined by a strong capture asymmetry ($k < 0.005$), and the state B exhibiting a deeper energy level and weaker asymmetry ($k > 0.01$). For the sample with the lowest doping concentration ($n_0 = 3.3 \times 10^{14}$ cm⁻³), the first defect preferential configuration is state B on the whole T -range investigated. For the samples with intermediate doping ($n_0 = 4.1$ and 4.8×10^{14} cm⁻³), the state transition from A to B is triggered at $T = 60$ °C and 75 °C, respectively. For the sample with the highest doping level ($n_0 = 9.6 \times 10^{14}$ cm⁻³), the preferential configuration remains at state A for the whole range of temperatures investigated. It seems that this transition is T promoted but first and foremost favored by low doping levels.

The relative standard deviation used to estimate the most likely defect energy is also presented in Fig. 8. Depending on

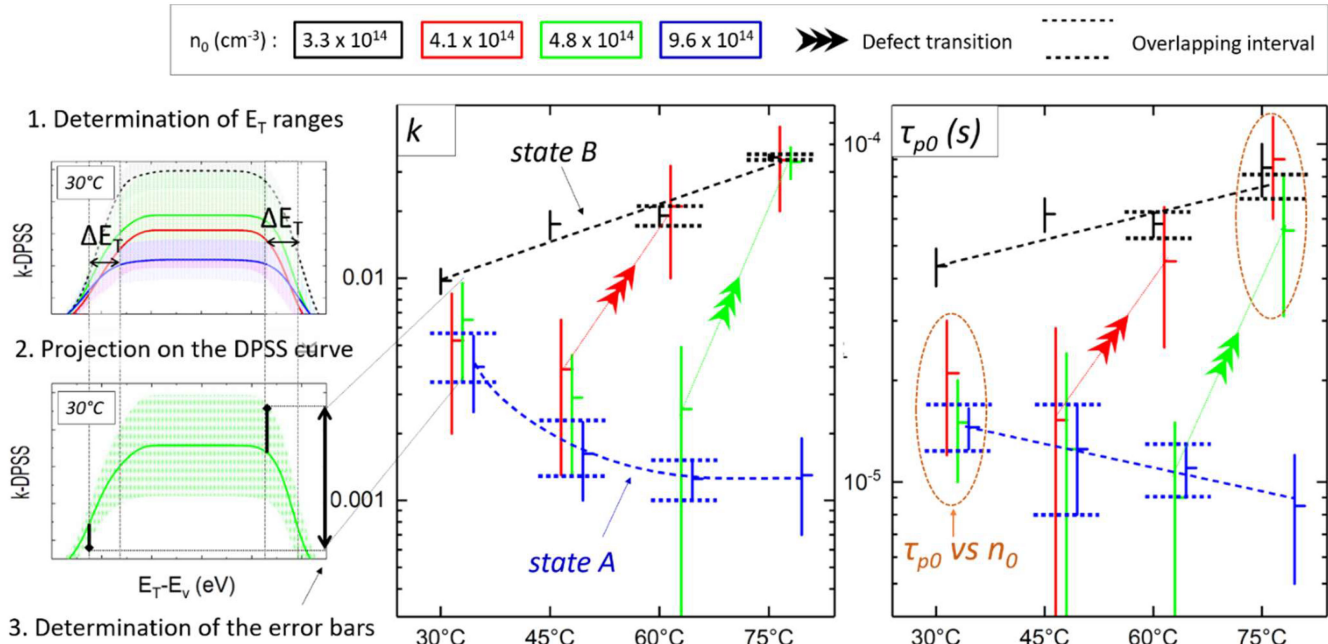


Fig. 9. (Left) Example of the approach used to determine the SRH parameters error bars is given for $T = 30^\circ\text{C}$ and $n_0 = 4.8 \times 10^{14} \text{ cm}^{-3}$. (center and right) The variation of k and τ_{p0} determined from n_0 -IDLS-based DPSS with temperature in the [30–75 °C] range highlights different behaviors depending on n_0 : lowly doped samples (black symbols) follow the state B, highly doped samples (blue symbols) follow the state A; samples with intermediate n_0 (red and green symbols) shift from A to B when T increases.

TABLE I
DEFECT PARAMETERS OBSERVED IN THIS WORK

Room-T n_0 -IDLS results			Temperature-dependent results in the [30–75]°C range		
	k	E_T-E_v (eV)		k	E_T-E_v (eV)
1 st defect	0.007 ± 0.001	0.39 ± 0.09	<i>state B</i>	$[0.010-0.035]$	0.40 ± 0.02 or 0.60 ± 0.02
		0.68 ± 0.06	<i>state A</i>	$[0.0040-0.0013]$	0.31 ± 0.03 or 0.63 ± 0.04
2 nd defect	0.60 ± 0.03	0.23 ± 0.03		-	
		0.90 ± 0.02			

the T considered, the RSD for either state A or B is plotted. We could extract the most likely energy (E_T) of the first defect from the RSD local minima: $E_v + 0.31 \pm 0.03 \text{ eV}$ (or $0.63 \pm 0.04 \text{ eV}$) for state A against $E_v + 0.40 \pm 0.02 \text{ eV}$ (or $0.60 \pm 0.02 \text{ eV}$) for state B. By studying separately these two possible states, we are now able to deliver more relevant (E_T ; k) values for the first defect than the preliminary ones, which were based on lifetime dependence to $1/n_0$ at room- T , and were actually altered by the coexistence of state B (governing the lowest n_0 sample) and state A (governing the others).

With the four n_0 conditions screened here, obtaining a DPSS intersection for both defect configurations concomitantly was not possible for each temperature. We assumed that the energy position was negligibly impacted. Consequently, when the DPSS intersection could not be experimentally observed, we had the energy positions (and associated uncertainties) projected on the isolated DPSS of interest and we could even so estimate (k ; τ_{p0}). Presenting the (k ; τ_{p0}) set of SRH parameters

this way (see Fig. 9) illustrates well the aforementioned defect transition from state A to B. For determining the k (or τ_{p0}) related error bars, we considered the maximal uncertainty introduced by DPSS error bands, as exemplified by the green DPSS curve in Fig. 9 for $T = 30^\circ\text{C}$ and $n_0 = 4.8 \times 10^{14} \text{ cm}^{-3}$.

When DPSS indeed intersect, the interval for which DPSS overlap was used to refine k and τ_{p0} uncertainties. Focusing on samples with a constant defect configuration over T (i.e., $n_0 = 3.3 \times 10^{14} \text{ cm}^{-3}$ and $n_0 = 9.6 \times 10^{14} \text{ cm}^{-3}$) allows to comment on the variation of the mean values of k and τ_{p0} with T . When state B is at play, both k and τ_{p0} increase steadily with temperature from 0.010 to 0.035 and from 44 to 85 μs , respectively. When state A dominates, both parameters are decreasing: τ_{p0} decrease is linear (14 to 9 μs), while k follows a power law ($T^{-1.6}$) from 0.0040 to 0.0013. As aforementioned, the samples with intermediate n_0 values shift from A to B as T increases.

We initially planned to compare n_0 -IDLS- and T -IDLS-based DPSS results in order to determine which of the two solutions

is more likely. Nonetheless, after highlighting that both k and τ_{p0} were T dependent and each parameter T -dependence is also influenced by n_0 , it seems risky to further look into T -IDLS-based DPSS. The equivalence of samples compositional properties was questioned in Section II-B. The defect state transition triggered by temperature reduces the possibilities of evaluating the n_0 -dependence of τ_{p0} to only two temperatures (30 and 75 °C) with, in each case, three n_0 conditions, as highlighted by the orange circles in Fig. 9. τ_{p0} shows an overall decrease of comparable amplitude for A ($T = 30$ °C) and B states ($T = 75$ °C), which corresponds to an increase of the average N_T by a factor of 1.4 and 1.49, respectively. Such a variation can be seen as small and could support the hypothesis of a weak dependence of N_T with the sample location and related n_0 . Nonetheless, as τ_{p0} error bars are quite large, even larger than the actual τ_{p0} variations, this statement still needs to be confirmed.

IV. CONCLUSION

This article aimed at identifying the SRH parameters of defects dominating τ_{bulk} in the dislocation-rich regions of cast-mono wafers. This article is based on the use of intentionally compensated cast mono, featuring a strong variation of n_0 along the region of interest (i.e., rich in dislocations). We showed by applying the defect isolation procedure that the SRH lifetime could be described by the contributions of two independent single-level defects. The first defect features a positive slope ($d\tau_D/dY$) and dominates the low-injection SRH lifetime. The second defect features a negative slope and dominates the SRH lifetime at medium- and high-injection levels. The first estimation of these defects symmetry factors k is given in Table I at nearly room- T (30 °C). Additional defects are possibly involved in SRH recombination but the present method does not allow to isolate accurately other defects than the two prominent ones. Exploiting lifetime data collected at temperatures ranging from 30 to 75 °C allowed to build k - and τ_{p0} -DPSS curves for samples with similar crystallographic properties but different n_0 . The first and second defects exhibited, respectively, a continuous and split range DPSS whatever the n_0 or T considered. The further characterization of the SRH parameters was restricted to the first defect only. The comparison of DPSS outputs at different T evidenced two possible configurations for the first defect: a state B, favored by high T and low n_0 , and a state A, conversely predominant at low T and high n_0 . The samples with the lowest and highest n_0 values considered here exhibit a constant state over the T -range investigated. On the other hand, for the samples with intermediate n_0 , the first defect shifts from state A to B when T increases. The higher the n_0 , the higher the threshold temperature. The precise mechanism behind the first defect transition remains unclear. The postulate of independent discrete single-level defects ruling SRH is questioned by this result that may indicate the presence of a multivalent defect. The output SRH parameters (E_T ; k) obtained in this article are reported in Table I.

Although this set of data does not allow to state the precise nature of the defects at play, it can be used for describing

carrier recombination, for instance, in numerical simulations for PV devices on cast mono. None of the first and second defects detected are likely to correspond to one specific dissolved impurity and should rather be seen as “apparent” responses involving multiple subcontributions. For completeness, we can cite substitutional gold (Au_s) [26] and silicon oxide precipitates [27] as impurities associated with k values in the range of what we observed for the first defect. It should be pointed out that only the isolation process uncertainty was considered here. As a consequence, the reported defect transition would still need to be confirmed, when other contributions to the total uncertainty (such as the determination of dopant concentrations, the intrasample lifetime nonuniformity, and the impact of S) are taken into account. A focus on the second defect would be of interest as this defect governs the SRH lifetime over a broad range of excess carrier densities. Obtaining continuous DPSS for the second defect would serve this purpose and could be facilitated by the investigation of a wider range of temperatures. Since the simplified SRH statistics considers independent discrete levels and is a rather point-like defect oriented, a complementary study of dislocation-rich cast mono by more sophisticated models is worth considering. For example, a recombination model was proposed in [28] for precipitate-related lifetime studies.

REFERENCES

- [1] Y. Lv *et al.*, “Towards high-efficiency industrial p-type monolike Si PERC solar cells,” *Sol. Energy Mater. Sol. Cells*, vol. 204, Jan. 2020, Art. no. 110202.
- [2] M. Kivambe *et al.*, “Record-efficiency n-type and high-efficiency p-type monolike silicon heterojunction solar cells with a high-temperature gettering process,” *ACS Appl. Energy Mater.*, vol. 2, no. 7, pp. 4900–4906, Jun. 2019.
- [3] H. C. Sio *et al.*, “The electrical properties of high performance multicrystalline silicon and mono-like silicon: Material limitations and cell potential,” *Sol. Energy Mater. Sol. Cells*, vol. 201, Oct. 2019, Art. no. 110059.
- [4] T. Ervik, G. Stokkan, T. Buonassisi, Ø. Mjøs, and O. Lohne, “Dislocation formation in seeds for quasi-monocrystalline silicon for solar cells,” *Acta Materialia*, vol. 67, pp. 199–206, Apr. 2014.
- [5] V. A. Oliveira *et al.*, “Cellular dislocations patterns in monolike silicon: Influence of stress, time under stress and impurity doping,” *J. Cryst. Growth*, vol. 489, pp. 42–50, May 2018.
- [6] M. Trempa *et al.*, “Dislocation formation in seed crystals induced by feedstock indentation during growth of quasimono crystalline silicon ingots,” *J. Cryst. Growth*, vol. 454, pp. 6–14, Nov. 2016.
- [7] A. Samadi *et al.*, “Hydrogenation of dislocations in p-type cast-mono silicon,” *AIP Conf. Proc.*, vol. 2147, no. 1, Aug. 2019, Art. no. 140007.
- [8] B. J. Hallam *et al.*, “Development of advanced hydrogenation processes for silicon solar cells via an improved understanding of the behaviour of hydrogen in silicon,” *Prog. Photovolt.*, vol. 28, pp. 1217–1238, Dec. 2020, doi: [10.1002/pip.3240](https://doi.org/10.1002/pip.3240).
- [9] C. Sun *et al.*, “Transition metals in a cast-monocrystalline silicon ingot studied by silicon nitride gettering,” *Phys. Status Solidi*, vol. 13, no. 12, Dec. 2019, Art. no. 1900456, doi: [10.1002/pssr.201900456](https://doi.org/10.1002/pssr.201900456).
- [10] D. Tweddle *et al.*, “Atom probe tomography of fast-diffusing impurities and the effect of gettering in multicrystalline silicon,” *AIP Conf. Proc.*, vol. 1999, no. 1, Aug. 2018, Art. no. 130019.
- [11] J. Schmidt, P. Pohl, K. Bothe, and R. Brendel, “Advances in contactless silicon defect and impurity diagnostics based on lifetime spectroscopy and infrared imaging,” *Adv. Optoelectron.*, vol. 2007, Apr. 2007, Art. no. 092842.
- [12] I. E. Bondarenko, O. V. Kononchuk, and V. Sirokin, “Reconstruction of the recombination centre distribution in dislocation impurity atmosphere in Si,” *Solid State Phenomena*, vol. 51–52, pp. 123–130, May 1996.
- [13] K. Knobloch, M. Kittler, and W. Seifert, “Influence of contamination on the dislocation-related deep level C1 line observed in deep-level-transient spectroscopy of n-type silicon: A comparison with the tech-

- nique of electron-beam-induced current," *J. Appl. Phys.*, vol. 93, no. 2, pp. 1069–1074, Jan. 2003.
- [14] S. Rein, "Theory of lifetime spectroscopy," in *Lifetime Spectroscopy: A Method of Defect Characterization in Silicon for Photovoltaic Applications*. Berlin, Germany: Springer, 2005, ch. 3, sec. 3.3.2, pp. 102–107.
- [15] H. Haug, R. Søndenå, A. Berg, and M. S. Wiig, "Lifetime spectroscopy with high spatial resolution based on temperature and injection dependent photoluminescence imaging," *Sol. Energy Mater. Sol. Cells*, vol. 200, Sep. 2019, Art. no. 109994.
- [16] J. Schmidt *et al.*, "Atomic-layer-deposited aluminum oxide for the surface passivation of high-efficiency silicon solar cells," in *Proc. 33rd IEEE Photovolt. Spec. Conf.*, San Diego, CA, USA, 2008, pp. 1–5, doi: [10.1109/PVSC.2008.4922636](https://doi.org/10.1109/PVSC.2008.4922636).
- [17] V. Grivickas, D. Noreika, and J. A. Tellefson, "Surface and Auger recombination in silicon wafers of high carrier density," *Lithuanian Phys. J.*, vol. 29, no. 5, pp. 48–53, 1989.
- [18] G. Coletti *et al.*, "Effect of iron in silicon feedstock on p- and n-type multicrystalline silicon solar cells," *J. Appl. Phys.*, vol. 104, no. 10, Nov. 2008, Art. no. 104913, doi: [10.1063/1.3021355](https://doi.org/10.1063/1.3021355).
- [19] D. Macdonald, A. Cuevas, A. Kinomura, Y. Nakano, and L. J. Geerligs, "Transition-metal profiles in a multicrystalline silicon ingot," *J. Appl. Phys.*, vol. 97, no. 3, Jan. 2005, Art. no. 033523, doi: [10.1063/1.1845584](https://doi.org/10.1063/1.1845584).
- [20] J. Veirman *et al.*, "Hall mobility reduction in single-crystalline silicon gradually compensated by thermal donors activation," *Solid-State Electron.*, vol. 54, no. 6, pp. 671–674, Jun. 2010.
- [21] E. Ohta and M. Sakata, "Temperature dependence of Hall factor in low-compensated n-type silicon," *Jpn. J. Appl. Phys.*, vol. 17, no. 10, pp. 1795–1804, Oct. 1978.
- [22] F. Schindler *et al.*, "Towards a unified low-field model for carrier mobilities in crystalline silicon," *Sol. Energy Mater. Sol. Cells*, vol. 131, pp. 92–99, Dec. 2014.
- [23] L. C. Kimerling and J. L. Benton, "Electronically controlled reactions of interstitial iron in silicon," *Physica B+C*, vol. 116, pp. 297–300, Feb. 1983.
- [24] F. E. Rougieux *et al.*, "Acceptor-related metastable defects in compensated n-type silicon," presented at the 22nd Int. Photovolt. Sci. Eng. Conf., Hangzhou, China, Nov. 2012, pp. 1–6.
- [25] S. Dubois *et al.*, "Effect of intentional bulk contamination with iron on multicrystalline silicon solar cell properties," *J. Appl. Phys.*, vol. 102, no. 8, Oct. 2007, Art. no. 083525.
- [26] D. Macdonald and L. J. Geerlings, "Recombination activity of interstitial iron and other transition metal point defects in p- and n-type crystalline silicon," *Appl. Phys. Lett.*, vol. 85, no. 18, Nov. 2004, Art. no. 4061, doi: [10.1063/1.1812833](https://doi.org/10.1063/1.1812833).
- [27] J. D. Murphy, K. Bothe, R. Krain, V. V. Voronkov, and R. J. Falster, "Parameterisation of injection-dependent lifetime measurements in semiconductors in terms of Shockley-Read-Hall statistics: An application to oxide precipitates in silicon," *J. Appl. Phys.*, vol. 111, Jun. 2012, Art. no. 113709.
- [28] W. Kwapił, J. Schön, W. Warta, and M. C. Schubert, "Carrier recombination at metallic precipitates in p-and n-type silicon," *IEEE J. Photovolt.*, vol. 5, no. 5, pp. 1285–1292, Sep. 2015.